Oxygen vacancy ordering induced displacements of cations in yttria-stabilized zirconia

Yanguo Wang, Canying Cai, Liang Li, Li Yang, Yichun Zhou, and Guangwen Zhou

Citation: AIP Advances **6**, 095113 (2016); doi: 10.1063/1.4963202
View online: http://dx.doi.org/10.1063/1.4963202
View Table of Contents: http://scitation.aip.org/content/aip/journal/adva/6/9?ver=pdfcov
Published by the AIP Publishing

Oxygen vacancy ordering induced displacements of cations in yttria-stabilized zirconia

Yanguo Wang,[1] Canying Cai,[1] Liang Li,[2] Li Yang,[1] Yichun Zhou,[1,a] and Guangwen Zhou[2,a]

[1]*School of Materials Science and Engineering and Key Laboratory of Low Dimensional Materials and Application Technology of Ministry of Education, Xiangtan University, Xiangtan 411105, China*

[2]*Department of Mechanical Engineering and Materials Science and Engineering Program, State University of New York at Binghamton, New York 13902, USA*

(Received 24 June 2015; accepted 9 September 2016; published online 16 September 2016)

Using scanning transmission electron microscopy, we report direct observation of oxygen vacancy ordering induced atomic displacements of the cation sub-lattice in yttria-stabilized zirconia (YSZ). We find that the cation lattice adopts a zigzag configuration along the [100] direction with alternately narrow and wide lattice spacings equivalent of 0.85 and 1.15 times of the (200) inter-planar distance of the cubic YSZ. Using atomistic simulations, we show that the cation displacements are induced by the alternate presence of oxygen vacancies at the (1/4, 1/4, 1/4) and (1/4, 3/4, 1/4) sites of the unit cells in the [001] direction. The results demonstrate that significant enrichment of yttrium atoms can occur within individual YSZ grains in addition to the typical surface or grain boundary segregation of dopant atoms. [http://dx.doi.org/10.1063/1.4963202]

I. INTRODUCTION

Nonstoichiometry in oxide materials is a persistent phenomenon with large influence on their physical and chemical properties. For example, extrinsic generation of oxygen vacancies in ZrO_2 upon doping with other oxides such as Y_2O_3 can stabilize the metastable cubic fluorite structure at room temperature (i.e., yittria-stabilized zirconia, YSZ) with improved mechanical, thermal, and ionic conductivity properties.[1,2] Detailed knowledge on the spatial distribution of oxygen vacancies is critically important for predicting and designing oxide materials with tailored properties. However, a quantitative determination of oxygen vacancies in low concentrations, especially with spatial resolution, has traditionally been difficult. Transmission electron microscopy (TEM) has been widely used to characterize the atomic structure of materials. However, TEM imaging of an oxygen sub-lattice is challenging due to its relative low scattering power and the complex convolution of TEM focus condition and sample thickness. Scanning TEM (STEM) techniques have progressed dramatically in recent years in imaging individual atoms and defects with the implementation of aberration correction and new algorithms.[3–6] Using aberration corrected STEM, the lattice distortions in materials can now be measured on a unit-cell by a unit-cell basis and at the picometer level.[7–9] The clear view of atom positions enables direct comparison of experiment with theory modeling.[7,8,10–12] In this work, we employ the contrast based on the high-angle scattering of electrons (Z-contrast) in a STEM mode to image the cation sub-lattice only, which allows for directly measuring vacancy-induced displacements of cations in YSZ. In conjunction with density-functional theory (DFT) calculations, we show that the location and concentration of oxygen vacancies in YSZ can be determined from the measured atomic displacements of the cation sub-lattice.

[a]To whom correspondence should be addressed: zhouyc@xtu.edu.cn (Y. Zhou); gzhou@binghamton.edu (G. Zhou)

ZrO_2 is chosen for the study because of its technological importance spanning from thermal barrier coating, heterogeneous catalysis, to semiconductor devices. Properties of ZrO_2 for these applications rely critically on the equilibria and atomic structure of the oxide. Pure zirconia exists in three polymorphs: monoclinic structure up to a temperature of ~ 1446 K, where it changes to the tetragonal modification, and finally the cubic fluorite structure at temperatures higher than 2643 K. The high-temperature metastable phases are the most interesting from the point of view of their properties and technological importance. The addition of Y_2O_3 stabilizes the high-temperature forms at low temperatures with the concomitant introduction of oxygen vacancies for charge compensation. The idealized structure of cubic-YSZ has a fluorite-type structure in which Y and Zr atoms randomly occupy face-centered cubic (FCC) sites while oxygen atoms reside at tetrahedral (1/4, 1/4, 1/4)-type interstitial sites.[13] The presence of oxygen vacancies causes relaxation of ions away from their regular fluorite lattice positions.[14–16] The nature of the defect-induced atomic displacements has been a controversial topic for some time. The directions of <110>[17] or <111>[18–20] were proposed for the displacements of cations, and the direction of <100>,[15,19–21] <111>,[20,22–24] or both[15,18] were suggested for the relaxations of anions. Such a controversy can be attributed to the difficulty in characterizing experimentally the distribution of vacancies, cations and anions in YSZ at the atomic scale as well as the coupling of the relaxation of both cations and anions. Using aberration-corrected STEM to decouple the relaxation of cations and anions, we determine unambiguously the atomic displacements associated with the cation sub-lattice only. The atomic-scale experimental observations provide experimental input to DFT modeling, which allows for identifying the spatial distribution of oxygen vacancies.

II. EXPERIMENTAL AND COMPUTATION METHODS

Zirconia doped with 7 wt.% (3.7 mol.%) Y_2O_3 was grown on a polycrystalline alumina substrate held at 1000 °C via electron-beam physical vapor deposition. The grown YSZ was annealed in a muffle furnace at 1150 °C for 24 hours with the heating and cooling rates set at 10 °C/min. TEM specimens were made by first cutting the annealed YSZ into small pieces and were mechanically thinned to about 5-10 μm, followed by Argon ion milling (Gatan, Model 691). The TEM samples were characterized using an aberration-corrected ARM-200 transmission electron microscope (TEM) operated at an accelerating voltage of 200 kV. STEM imaging was performed with the camera length set at 8 cm corresponding to an inner collection angle of 68 mrad. Simulations for the high angle annular dark field (HAADF) images were conducted using the xHREM program package with the inner and outer collection angles of 68 mrad and 150 mrad along with other simulation parameters carefully matched to the experimental conditions. The electron diffraction patterns of the DFT relaxed defected ZrO_2 structure were simulated by performing dynamical electron diffraction calculation using the multislice method, where atom positions and lattice parameters of the unit cell were based on the DFT calculations. The DFT calculations were performed using the Vienna ab-initio simulation package (VASP)[25,26] with the local density approximation (LDA)[27] exchange-correlation functional and projector augmented wave (PAW) pseudopotentials,[28] in conjunction with a planewave cutoff energy of 400 eV. A 2×2×2 supercell was used in the calculations. The experimentally measured lattice parameter of 5.20 Å is adopted for the unit cell. The Γ point was used to sample the Brillouin zone, and all atoms were allowed to move during the relaxation. The Brillouin-zone sampling scheme, cell size and cut-off energy adopted in our calculation are similar as the previous studies.[29,30]

III. RESULTS AND DISCUSSION

Fig. 1(a) is a typical bright field (BF) TEM image of the annealed YSZ sample, where the YSZ grain is oriented along the [001] zone axis. The BF image shows a relatively uniform contrast across the grain. However, two-dimensional (2D) lattice can be found in some small areas (~ 5 nm in lateral size). As indicated by the red circles in Fig. 1(a), the lattice spacing of the 2D lattice is ~ 5 Å. Fig. 1(b) is a representative [001] selected area electron diffraction (SAED) pattern obtained from the majority area of the grain, which can be indexed well with the fluorite-like cubic YSZ. The lattice constant derived from the SAED pattern is ~ 0.52 nm, consistent with the reported value of the cubic

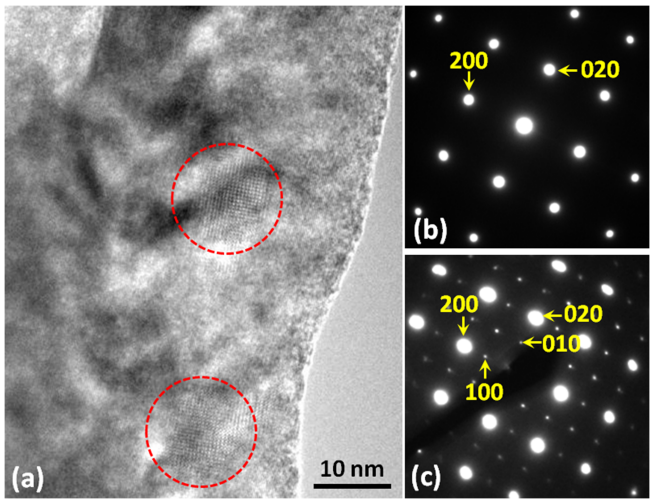

FIG. 1. (a) Bright field TEM image showing the typical microstructure of the annealed YSZ grain, where the presence of superlattice regions in the matrix of the cubic phase is indicated by red circles; (b) SAED pattern taken along the [001] zone axis of the cubic YSZ showing the presence of the basic reflections only; (c) SAED pattern taken from the ordered region showing the presence of superlattice.

phase of YSZ.[31] Fig. 1(c) shows a typical [001] SAED pattern obtained from the 2D lattice regions (e.g., the regions indicated with the red circles in Fig. 1(a)). In addition to the (200) and (220)-type fundamental reflections associated with the fluorite structure of the cubic YSZ, Fig. 1(c) shows the (100)- and (010)-type extra spots. In the cubic fluorite structure, Zr and Y atoms are randomly located at the face-centered cubic (FCC) lattice sites. The presence of the {010}-type forbidden reflections of the FCC lattice in the 2D lattice region suggests that the cubic fluorite structure undergoes locally disorder → order transition, for which Zr and Y atoms occupy the regular lattice sites of the unit cell of the L10 ordered structure.[16,32]

In order to reveal the atomic structure of the regions having the superlattice reflections, HAADF imaging was performed using aberration-corrected STEM. Fig. 2 is a typical HAADF-STEM image obtained from the regions showing the superlattice reflections in the SAED pattern (e.g., the Fig. 1(c) and the regions indicated with the red circles in Fig. 1(a)). The signal scattered by oxygen atoms is at a lower angle compared to that by Zr and Y atoms and thus cannot be collected by the high-angle annular detector. Consequently, the contrast in the HAADF-STEM image is produced by Zr and Y atoms and the white image dots in Fig. 2(a) correspond to the positions of Zr and Y atomic columns viewed along the [001] direction of the YSZ grain. It is worthy of noting that the presence of Y atoms in the ZrO_2 lattice does not give rise to noticeable variation in image contrast for their close atomic number to that of Zr (Zr = 40 vs. Y = 39).

The HAADF image shown in Fig. 2(a) can be divided into disordered and ordered regions and their approximate boundary is marked by the dashed lines. On the left side is the perfect cubic fluorite structure, and on the right side corresponds to the region that shows the superlattice reflections in the electron diffraction pattern. The image dots of the cubic YSZ along the [100] and [010] directions form a square configuration with the four-fold rotation symmetry. Fig. 2(b) shows the intensity profile of the image dots of the cubic region marked by the yellow rectangle in Fig. 2(a), from which the distance between the neighboring image dots is measured to be 0.26 nm (the error bar is 0.005 nm) along the [100] direction. The intensity profile of the image dots along the [010] direction of the perfect cubic region gives the similar distance (0.26 nm) between neighboring image dots. Therefore, the lattice constant of the cubic phase in the cubic region is 0.52 nm, which is consistent with the value derived from the SAED pattern shown in Fig. 1(b).

Shift of the image dots from the cubic lattice sites can be discerned in the region that has superlattice reflections. Careful examination of the HAADF image of Fig. 2(a) shows that the image dots shift along both the [100] and [010] directions in the region on the right side of the marked dashed line. As indicated in Fig. 2(a), the shift of the image dots along the [100] direction makes the

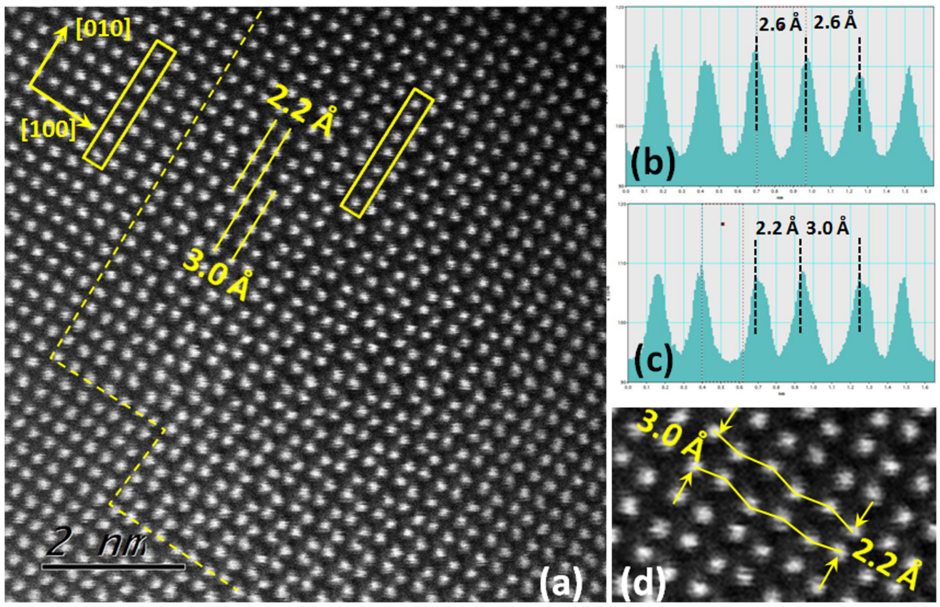

FIG. 2. (a) HAADF-STEM image shows the arrangement variation of the image dots at superlattice area (ordered YSZ) with respect to the cubic structure (disordered YSZ), where the dashed lines show the boundary between the ordered and disordered regions.(b) Profiles of image dots in the cubic region; (c) Profiles of image dots in the superlattice region. (d) Zoom-in view of the superlattice region showing the zigzag configuration of cations along the [100] direction.

(200) planar spacings changing alternately between the values of 2.2 Å and 3.0 Å, which are equal to 0.85 and 1.15 times of the (200) inter-planar distance of the cubic phase and equivalent to an increase and decrease of 0.08 times of the lattice constant a of the perfect cubic ZrO_2 unit cell for the wide and narrow (200) planes (i.e., ± 0.08a). Fig. 2(c) is the intensity profile of the shifted image dots along the [010] direction as marked by the yellow rectangle in the middle region on the right side of the marked dashed line in Fig. 2(a), which shows that the distance between the nearest neighboring image dots is no longer equal. Instead, the distances between the neighboring dots become alternately closer and wider along the [010] direction. The narrow and wide spacings between the adjacent shifted dots are 2.2 Å and 3.0 Å, which are equal to 0.85 and 1.15 times of the (020) inter-planar distance of the cubic phase, respectively. Different from the [100] direction, the adjacent image dots along the [010] direction shift alternately in the opposite direction by the amount of ± 0.08a of the cubic ZrO_2 unit cell. This results in a zigzag arrangement of the image dots along the [100] direction in the ordered region, as shown in the zoom-in view (Fig. 2(d)). Despite the shifts of the cations along the [100] and [010] directions, the (100) and (010) lattice spacings remain the same as the cubic phase (i.e., 0.52 nm), suggesting that the cubic lattice is still retained in the region that shows superlattice reflections.

To augment the experimental measurements, we employ DFT to elucidate the origin of the atomic displacements. When Y_2O_3 is doped into ZrO_2, for every two Y^{3+} ions replacing two Zr^{4+} ions, one oxygen vacancy is generated to maintain charge neutrality, for which the oxide stoichiometry formula can be written as $Zr_2Y_2O_7$. The supercell in our DFT calculations is made of eight unit cells of the L10 ordered structure with one oxygen vacancy in each unit cell. Fig. 3 shows the atomic configuration of the structure, in which the two types of octants are arranged such that they alternate in the [001] direction of the unit cell. The type-I octant has the oxygen vacancy located at the (1/4, 1/4, 1/4) site while the type-II octant has the oxygen vacancy at the (1/4, 3/4, 1/4) site. Such an ordered arrangement of the oxygen vacancies provides the best match with the experimental results as detailed below.

We have performed DFT calculations of the $Zr_2Y_2O_7$ structure with the ordered distribution of oxygen vacancies in the way shown in Fig. 3 for quantitatively comparing with the atomic displacements measured from the experimental results. Fig. 4(a) is a [001] projection view of the minimum-energy structure obtained in the DFT calculations, where oxygen atoms are hidden for

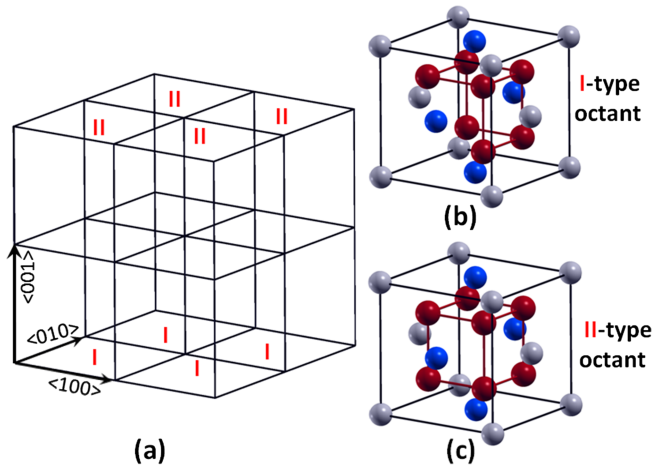

FIG. 3. (a) Supercell consisting of eight unit cells of the fluorite cubic structure, in which the two types of octants are arranged alternately in the [001] direction of the unit cell. (b) The type I octant has an oxygen vacancy at the (1/4, 1/4, 1/4) site. (c) The type II octant has an oxygen vacancy at the (1/4, 3/4, 1/4) site. Zr atoms are depicted by grey balls, Y by blue balls, and O by red balls.

better comparison with experiments because oxygen atoms do not show up in the HAADF images. It can be seen that the spacings between neighboring [010] rows of cations (which correspond to the (200) interplanar spacings) vary alternately in the values of 2.82 Å and 2.38 Å with a periodicity of 5.2 Å. These values are close to the experimentally measured (200) spacings of 3.0 Å and 2.2 Å shown in Fig. 2(a). The DFT calculations also show that neighboring cations in the [010] direction displace in opposite directions, which results in the zigzag configuration of the cations along the [100] direction. The distances between neighboring cations are alternately 2.83 Å and 2.37 Å with a periodicity of 5.2 Å. The DFT-obtained minimum structure is used to simulate STEM images for direct comparison to the experiment. The atomic displacements and the zigzag configurations in the simulated HAADF image (Fig. 4(b)) match well with the experimental HAADF image as shown in Fig. 4(c). Further supporting evidence for the proposed structure model shown in Fig. 3 is contained in the electron diffraction patterns. We have simulated the dynamical electron diffraction pattern using the DFT-relaxed minimum-energy structure. Fig. 4(d) shows the calculated electron diffraction pattern along the [001] zone axis, in which weak diffraction maxima corresponding to the positions of {100} planes are visible in addition to the fundamental diffraction {200} spots associated with the fluorite cubic structure, consistent with the experimentally observed electron diffraction pattern shown in Fig. 1(c).

Defect structure, in particular the distribution of vacancies in YSZ, has been a topic of long-standing controversy. It was suggested that oxygen vacancies have a strong tendency to form pairs in cubic YSZ with a variety of pairing directions such as <1 0 0>,[33] <1 1 1>,[34–36] <1 1 2>,[37] and <1 $\frac{1}{2}$ 0>.[38] Our DFT calculations indicate that none of these vacancy configurations reproduces the experimentally observed distortion of the cation sub-lattice shown in Fig. 2. Instead, we find that the alternate presence of oxygen vacancies at the (1/4, 1/4, 1/4) and (1/4, 3/4, 1/4) sites along the [001] direction (as shown in Fig. 3) induces the atomic displacements of the cation sub-lattice that matches well with the experimental results as shown in Figs. 4(a, b). The cation displacements from the ideal FCC sites are related to the relaxation of the neighboring cations away from the vacancies. When an oxygen vacancy is created, the neighboring cations will repel each other because of Coulombic interactions, thereby resulting in larger distance between cations. The structure model shown in Fig. 3 has the stoichiometric ratio of $Zr_2Y_2O_7$ and contains 16 Zr atoms, 16 Y atoms, and 28 O atoms along with 8 oxygen vacancies. The oxygen atoms and the oxygen vacancies reside at the tetrahedral sites formed by the Zr and Y atoms. Fig. 5(a) shows the locations of the 8 oxygen-vacancy containing tetrahedrons, which are at the alternative interstitial sites of (1/4, 1/4, 1/4) and (1/4, 3/4, 1/4) of each cube quadrant of the supercell. Figs. 5(b, c) show the equilibrium structures for the perfect and oxygen-vacancy containing tetrahedrons obtained from our DFT calculations,

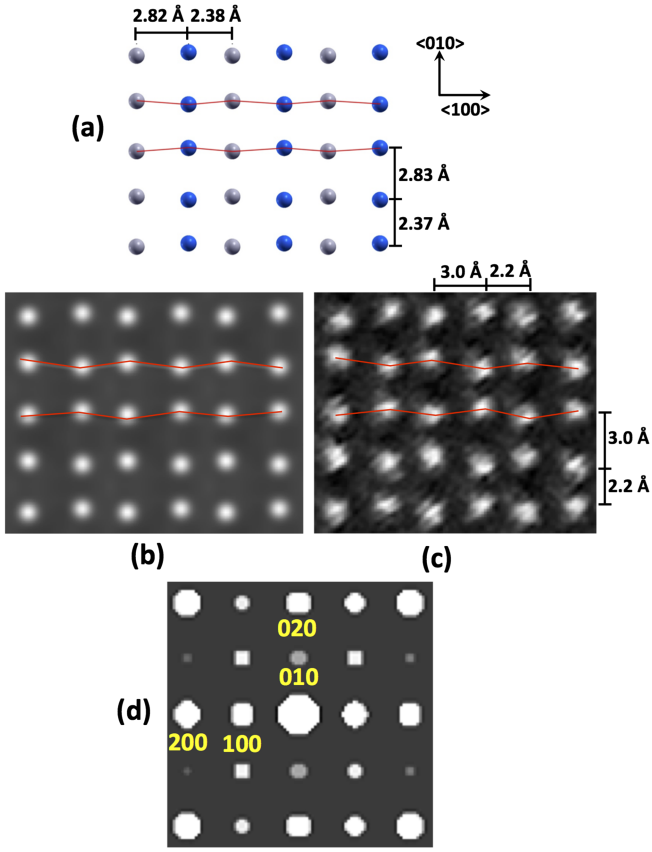

FIG. 4. (a) [001] projection view of the configuration of cations in the minimum-energy structure shown in Fig. 3, where oxygen atoms are hidden. (b) HAADF-STEM simulation image using the DFT-relaxed structure shown in (a). (c) experimental HAADF-STEM image showing the cation sub-lattice. (d) Simulated [001] zone electron diffraction pattern using the minimum-energy structure of the defected ZrO_2 shown in (a).

from which the six edges (i.e., the cation-cation bond lengths) of the tetrahedrons can be measured. As shown in Fig. 5(b), the oxygen-containing tetrahedron (corresponding to the fluorite structure of the cubic YSZ) has a cation-cation bond length of 3.68 Å. In contrast, the bond lengths for the

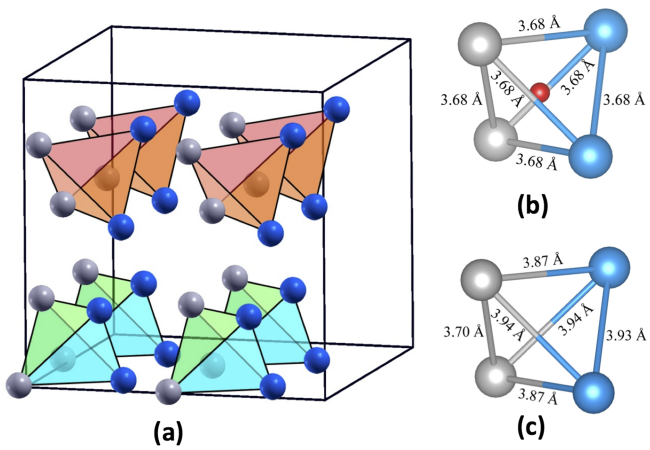

FIG. 5. (a) Oxygen-vacancy containing tetrahedrons in the equilibrium structure of $Zr_2Y_2O_7$ shown in Fig. 3 (Zr: grey balls, Y: blue balls), the presence of oxygen vacancies in the tetrahedrons causes the cations to repel each other by Coulombic interactions. Equilibrium cation-cation bond lengths for the oxygen-containing tetrahedron of the fluorite structure of the cubic YSZ (b) and for the oxygen-vacancy containing tetrahedron of the $Zr_2Y_2O_7$ structure (c).

defective tetrahedron (i.e., with an oxygen vacancy at the tetrahedral site for the $Zr_2Y_2O_7$ structure) are measured to be 3.94 Å, 3.94 Å, 3.93 Å, 3.87 Å, 3.87 Å, and 3.70 Å, respectively, all of which become increased compared with the oxygen-containing tetrahedron. The increased bond lengths can be attributed to the repulsive Coulombic interactions of neighboring cations owing to the missing of the tetrahedral oxygen atom.

Zirconia is one of the best corrosion-resistant and refractory materials and the properties of YSZ rely critically on the level of heterovalent dopants. While the influence of the formation of this yttria-rich phase on the properties of the parent zirconia is not clear, the significant enrichment of Y atoms in these local regions may induce instability of the high-temperature phases of YSZ. The crystal structure of zirconia undergoes phase transition from monoclinic to tetragonal and then to cubic at 1446 K and 2643 K, respectively. Small additions of Y_2O_3 are used to stabilize the high-temperature forms (either tetragonal or cubic) at low temperatures. When the dopant concentration is less than that required for the stabilized zirconia, then a mixture of monoclinic, tetragonal and cubic phases occurs.[39] The generation of monoclinic ZrO_2 within the parent high-temperature phase is harmful because the phase transition involves a volume change of 3-5%, leading to the coating failure for thermal barrier coating applications.[40] Yttria segregation to both external surfaces and grain boundaries has been observed for YSZ containing an Y_2O_3 level varying from 2 to 19 mol %.[41–45] As revealed from our STEM observation shown above, significant local enrichment of Y atoms can also occur within YSZ grains, where the concentration of Y in the L10 cation ordered regions ($Zr_2Y_2O_7$) increases to 50 mole % from the initial doping level of 3.7 mol % Y_2O_3. The nucleation and growth of Y-enriched regions in the grain can deplete Y in the surrounding area. Since the monoclinic phase is the thermodynamic phase for pure ZrO_2 at relatively low temperatures (< 1446 K), the Y-depleted region may tend to undergo the cubic → monoclinic phase transition. This will have detrimental consequences for the structure stability of the cubic phase of YSZ.

IV. CONCLUSION

In conclusion, we present combined atomic STEM imaging and DFT analysis of the local cation sub-lattice distortion in YSZ. We show that the cation sublattice adopts a zigzag configuration and alternately wide and narrow lattice spacings in the [100] direction. Using DFT calculations, we identify that these atomic displacements result from distortion of the cation tetrahedrons induced by the ordered distribution of oxygen vacancies alternate at the (1/4, 1/4, 1/4) and (1/4, 3/4, 1/4) of the unit cell. The formation of these oxygen vacancies is induced by the significant enrichment of Y atoms within the YSZ grain. The concentration and distribution of oxygen vacancies in the bulk play an important role in determining the ion conductivity which underlies many of the practical uses of YSZ. The insights gained here may be of importance for understanding the ionic transport properties of solid state conducting materials.

ACKNOWLEDGMENTS

This work was supported by the National Natural Science Foundation of China under Grant No 11274365 and the "Hundred Talents Program" of Hunan Province, China. The work at SUNY Binghamton was supported by the National Science Foundation under NSF CAREER Award Grant CMMI-1056611. This work used the Extreme Science and Engineering Discovery Environment (XSEDE), which is supported by National Science Foundation grant number OCI-1053575.

[1] M. Yashima, K. Ohtake, M. Kakihana, H. Arshi, and M. Yoshimura, J. Phys. Chem. Solids **57**(1), 17–24 (1996).
[2] C. Pascual and P. Duran, J. Am. Ceram. Soc. **66**, 23–27 (1983).
[3] D. A. Muller, N. Nakagawa, A. Ohtomo, J. L. Grazul, and H. Y. Hwang, Nature **430**, 657–661 (2005).
[4] S. J. Pennycook and P. D. Nellist, (Springer, New York, 2011).
[5] Y. M. Kim, J. He, M. D. Biegalski, H. Ambaye, V. Lauter, H. M. Christen, S. T. Pantelides, S. J. Pennycook, S. V. Kalinin, and A. Y. Borisevich, Nature Materials **11**, 888–894 (2012).
[6] J. An, J. S. Park, A. L. Koh, H. B. Lee, H. J. Jung, J. Schoonman, R. Sinclair, T. M. Gür, and F. B. Prinz, Sci. Rep. **3**, 2680 (2013).
[7] X. Sang, E. D. Grimley, C. Niu, D. L. Irving, and J. M. LeBeau, Appl. Phys. Lett. **106**, 061913 (2015).
[8] J. H. Dycus, J. S. Harris, X. Sang, C. M. Fancher, S. D. Findlay, A. A. Oni, T. E. Chan, C. C. Koch, J. J. L., L. J. Allen, D. L. Irving, and J. M. LeBeau, Microscopy and Microanalysis **21**(04), 946–952 (2015).

[9] A. A. Oni, X. Sang, S. V. Raju, S. Dumpala, S. Broderick, A. Kumar, S. Sinnott, S. Saxena, K. Rajan, and J. M. LeBeau, Appl. Phys. Lett. **106**, 011601 (2015).
[10] S. J. Pennycook, M. F. Chisholm, A. R. Lupini, M. Varela, A. Y. Borisevich, M. P. Oxley, W. D. Luo, K. van Benthem, S.-H. Oh, D. L. Sales, S. I. Molina, J. García-Barriocanal, C. Leon, J. Santamaría, S. N. Rashkeev, and S. T. Pantelides, Phil. Trans. Roy. Soc. A **367**, 3709–3733 (2009).
[11] I. MacLaren and Q. M. Ramasse, International Materials Reviews **59**(3), 115–131 (2014).
[12] Z. C. Wang, M. Saito, K. P. McKenna, L. Gu, S. Tsukimoto, A. L. Shluger, and Y. Ikuhara, Nature **479**, 380–383 (2011).
[13] *International Tables for Crystallography.* (Kluwer Academic Publisher, 1995).
[14] S. Hull, Rep. Prog. Phys. **67**, 1217 (2004).
[15] J. P. Goff, W. Hayes, S. Hull, M. T. Hutchings, and K. N. Clausen, Phys. Rev. B **59**(22), 14202–14219 (1999).
[16] J. C. Rao, Y. Zhou, and D. X. Li, J. Mater. Res. **16**(6), 1806–1813 (2001).
[17] T. R. Welberry, B. D. Butler, J. G. Thompson, and R. L. Withers, J. Solid State Chem. **106**, 46 (1993).
[18] D. Steele and B. E. Fender, J. Phys. C **7**, 1 (1974).
[19] M. Morinaga, J. B. Cohen and J. Faber, Jr., Acta Crystallogr., Sect. A: Cryst. Phys. Diffr., T heor. Gen. Crystallogr. **36**, 520 (1980).
[20] N. Ishizawa, Y. Matsushima, M. Hayashi, and M. Ueki, Acta Crystallogr., Sect. B: Struct. Sci. **55**, 726 (1999).
[21] D. N. Argyriou, M. M. Elcombe, and A. C. Larson, J. Phys. Chem. Solids **57**, 183 (1996).
[22] H. Horiuchi, A. J. Schulz, P. C. W. Leung, and J. M. William, Acta Crystallogr., Sect. B: Struct. Sci. **44**, 116 (1984).
[23] C. J. Howard, R. J. Hill, and B. E. Reichert, Acta Crystallogr., Sect. B: Struct. Sci. **44**, 116 (1988).
[24] C. M. Wang, S. Azad, S. Thevuthasan, V. Shutthanandan, D. E. McCready, and C. H. F. Peden, J. Mater. Res. **19**(5), 1315–1319 (2004).
[25] G. Kresse and J. Hafner, Phys. Rev. B **49**(20), 14251–14269 (1994).
[26] G. Kresse and J. Furthmuller, Comput. Mat. Sci. **6**, 15–50 (1996).
[27] J. P. Perdew and A. Zunger, Phys. Rev. B **23**, 5048–5079 (1981).
[28] G. Kresse and D. Joubert, Phys. Rev. B **59**(3), 1758–1775 (1999).
[29] A. Kushima and B. Yildiz, J. Mater. Chem. C **20**, 4809–4819 (2010).
[30] H. P. Ding, A. V. Virkar, and F. Liu, Solid State Ionics **215**, 16–23 (2012).
[31] M. Yashima, S. Sasaki, and M. Kakihana, Acta Crsytallogr.. Sect. B: Struct. Sci. **50**, 663–672 (1994).
[32] H. Kim, J. Y. Moon, J. H. Lee, J. K. Lee, Y. W. Heo, J. J. Kim, and H. S. Lee, J. Nanosci. Nanotechnol. **14**(10), 7961–7964 (2014).
[33] Z. R. Dai, Z. L. Wang, Y. R. Chen, H. Z. Wu, and W. X. Liu, Phil. Mag. A **73**(2), 415–430 (1996).
[34] J. P. Goff, W. Hayes, H. S. , M. T. Hutchings, and K. N. Clausen, Phys. Rev. B **59**, 14202 (1999).
[35] S. Ostanin, A. J. Craven, D. W. McComb, D. Vlachos, A. Alavi, A. T. Paxton, and M. W. Finnis, Phys. Rev. B **65**, 224109 (2002).
[36] A. Bogicevic and C. Wolverton, Phys. Rev. B **67**, 024106 (2003).
[37] A. Predith, G. Ceder, C. Wolverton, J. Persson, and T. Mueller, Phys. Rev. B **77**, 144104 (2008).
[38] P. Dalach, D. E. Ellis, and A. van de Walle, Phys. Rev. B **82**, 144117 (2010).
[39] C. G. Kontoyannis and M. Orkoula, J. Mater. Sci. **29**, 5316–5320 (1994).
[40] J. M. Drexler, A. L. Ortiz, and N. P. Padture, Acta Materialia **60**, 5437–5447 (2012).
[41] M. de Ridder, R. G. van Welzenis, A. W. Denier van der Gon, and H. H. Brongersma, J. Appl. Phys. **92**(6), 3056–3064 (2002).
[42] G. S. A. M. Theunissen, A. J. A. Winnubst, and A. J. Burggraaf, J. Mater. Sci. **27**, 5057 (1992).
[43] V. Vonk, N. Khorshidi, A. Stierle, and H. Dosch, Surf. Sci. **612**, 69–76 (2013).
[44] Y. Y. Lei, Y. Ito, and N. D. Browning, J. Am. Ceram. Soc. **89**(9), 2359–2363 (2002).
[45] J. A. Krogstad, R. M. Leckie, S. Kramer, J. M. Cairney, D. M. Lipkin, C. A. Johnson and L. C. G., J. Am. Ceram. Soc. **96**(1), 299–307 (2013).